Energy & Environmental Science

ROYAL SOCIETY OF CHEMISTRY

PAPER

View Article Online
View Journal | View Issue

Check for updates

Cite this: *Energy Environ. Sci.*, 2023, **16**, 2030

Asymmetric chloride-mediated electrochemical process for CO_2 removal from oceanwater†

Seoni Kim, [ac] Michael P. Nitzsche, [ab] Simon B. Rufer, [b] Jack R. Lake, [b] Kripa K. Varanasi *[b] and T. Alan Hatton *[a]

Received 25th November 2022,
Accepted 13th February 2023

DOI: 10.1039/d2ee03804h

rsc.li/ees

In recent years, the ocean has come to be recognized as a global-scale reservoir for atmospheric CO_2. The removal of CO_2 from oceanwater is thus considered a compelling approach to reduce ambient CO_2 concentrations, and potentially achieve net-negative emissions. As an effective means of oceanic CO_2 capture, we report an asymmetric electrochemical system employing bismuth and silver electrodes that can capture and release chloride ions by faradaic reactions upon application of appropriate cell voltages. The difference in reaction stoichiometry between the two electrodes enables an electrochemical system architecture for a chloride-mediated electrochemical pH swing, which can be leveraged for effective removal of CO_2 from oceanwater without costly bipolar membranes. With two silver–bismuth systems operating in tandem in a cyclic process, one acidifying the ocean water, and the other regenerating the electrodes through alkalization of the treated stream, CO_2 can be continuously removed from simulated oceanwater with a relatively low energy consumption of 122 kJ mol^{-1}, and high electron efficiency.

Broader context

Industrial emissions of carbon dioxide are wreaking havoc on the environment as the continuing accumulation of CO_2 in the atmosphere leads to rising temperatures and disruption of the global climate patterns. To mitigate this problem, in addition to reducing CO_2 emissions from point sources, much attention has been given to negative emissions technologies to remove carbon dioxide directly from the ambient environment, where the very dilute levels of CO_2 make removal challenging. The total amount of CO_2 emissions partitioning into the oceans rivals that retained by the atmosphere, and thus effective means for its removal could augment the other negative emissions technologies to reduce the environmental burden imposed by this greenhouse gas. Approaches to removing CO_2 from oceanwater rely on adjusting the water pH from about 8.1 to less than 7 to ensure that the speciation of dissolved inorganic carbon (DIC) from carbonates and bicarbonates is changed to molecular CO_2 which can then be stripped off under vacuum. It is desirable that approaches be identified that do not require addition of chemicals, nor lead to parasitic reactions with the formation of undesirable compounds. For this reason, electrochemical systems have been considered as good options for pH swing in oceanwater since, because the reactions are driven by supplying electrons in a controllable manner, we can avoid chemical use and parasitic reactions. Current studies on CO_2 removal from oceanwater have used bipolar membrane electrodialysis (BPMED), although the high cost of bipolar membranes might impede the commercialization of the process, and some of these architectures even present risks of toxic redox-couples leaking into the oceanwater. We propose a new approach based solely on electrochemical modulation of the pH to initially release the CO_2 and then to alkalize the treated water before it is returned to the ocean. This approach (i) does not require expensive membranes or addition of chemicals, (ii) is easy to deploy, (iii) does not lead to formation of byproducts or secondary streams, and (iv) requires a lower energy input (122 kJ mol^{-1}) than do other approaches, to the best of our knowledge. In addition, a preliminary technoeconomic analysis which suggests that this ocean capture system can be economically feasible.

Introduction

Industrial emissions of carbon dioxide and other gases are wreaking havoc on the environment as the continuing accumulation of CO_2 in the atmosphere leads to rising temperatures and disruption of the global climate patterns.[1,2] While much attention has been focused on strategies for mitigation of the global CO_2 release of almost 40 Gt per year through capture at point sources followed by geologic storage,[3–8] more recently there has been a surge of interest in negative emissions

[a] *Department of Chemical Engineering, Massachusetts Institute of Technology, Cambridge, MA 02139, USA. E-mail: tahatton@mit.edu*
[b] *Department of Mechanical Engineering, Massachusetts Institute of Technology, Cambridge, MA 02139, USA. E-mail: varanasi@mit.edu*
[c] *Department of Environmental Science and Engineering, Ewha Womans University, Seoul, 03760, Republic of Korea*

† Electronic supplementary information (ESI) available. See DOI: https://doi.org/10.1039/d2ee03804h

Open Access Article. Published on 13 February 2023. Downloaded on 12/27/2024 11:57:29 AM.
This article is licensed under a Creative Commons Attribution-NonCommercial 3.0 Unported Licence.

This journal is © The Royal Society of Chemistry 2023

Open Access Article. Published on 13 February 2023. Downloaded on 12/27/2024 11:57:29 AM.
This article is licensed under a Creative Commons Attribution-NonCommercial 3.0 Unported Licence.

technologies in which the offending gases (currently at an atmospheric concentration of ~415 ppm[9]) are removed from the ambient environment itself through approaches such as direct air capture (DAC),[10–15] bioenergy with carbon capture and sequestration (BECCS),[16–18] and reforestation.[19,20]

The focus on atmospheric accumulation has not yet been matched by a similar drive to reduce CO_2 in oceans and other surface waters, which, since the dawn of the industrial era, have acted as large-scale carbon sinks, absorbing 30–40% of anthropogenic CO_2 emissions.[21,22] The resulting increased acidification of ocean waters has already led to destruction of coral reefs,[23,24] and reduced carbonate ion concentrations harm shellfish and other marine life.[25,26] Since the total amount of CO_2 emissions partitioning into the oceans rivals that retained by the atmosphere, effective means for its removal could augment the other negative emissions technologies to reduce the environmental burden imposed by this greenhouse gas. The concentrations in oceanwater (on a volumetric basis) are much higher at 100 mg L^{-1} than that in the ambient air (0.77 mg L^{-1}),[27,28] and thus smaller volumes will need to be treated than in DAC, which could provide a processing advantage. Moreover, while direct air capture requires both capture of the CO_2 by chemical complexation with a sorbent, and subsequent breaking of these bonds when the CO_2 is recovered as a pure gas, only the latter step is needed for CO_2 removal from surface waters, which avoids one of the steps usually required for CO_2 mitigation from gaseous sources.[29–31]

Approaches to solving this challenging problem need to be identified that do not require addition of chemicals, nor lead to parasitic reactions with the formation of undesirable compounds. CO_2 from the air dissolves in seawater as carbonic acid, which speciates as bicarbonate and carbonate ions by releasing protons according to the reactions[32]

$$CO_2 + H_2O \rightleftarrows H_2CO_3 \rightleftarrows HCO_3^- + H^+ \quad (1)$$

$$HCO_3^- \rightleftarrows CO_3^{2-} + H^+ \quad (2)$$

Since this equilibrium is based on the proton concentration, the dissolved inorganic carbon (DIC) can be converted back to molecular CO_2 by simply lowering the pH of the ocean water; the CO_2 can be removed as a pure gas by stripping under vacuum. The pH of the treated water can then be raised before it is returned to the ocean, which has the benefit of countering the acidification of the oceans, and fostering the further absorption of CO_2 from the atmosphere. The discharge of the CO_2-depleted water into the ocean after treatment imposes significant limitations in choosing a method of altering pH.[29] For example, modulation of the pH through addition of acid or base raises concerns about residual chemicals affecting the marine ecosystem, as well as the added cost of chemical supplies. For this reason, electrochemical systems have been considered as good options for the pH swing of oceanwater due to their reversibility.[29,33,34] Since the reactions are driven by supplying electrons in a controllable manner, we can avoid chemical use and parasitic reactions.[31,35,36]

To date, two approaches have been proposed for electrochemically driven CO_2 removal from seawater: electro-deionization[30,34] and electrodialysis.[29,33,37–39] In the electro-deionization process, water splitting reactions generating hydrogen and oxygen gases occur at each electrode to modulate the pH, driving CO_2 removal from the oceanwater.[30,34] However, the high resistivity of the system and high overpotentials for the reactions lead to a high overall process energy consumption. In contrast, bipolar membrane electrodialysis (BPMED) provides a more energy-efficient means to dissociate water molecules.[33,38] The water dissociation catalysts embedded in a bipolar membrane enable decomposition of water molecules into protons and hydroxide ions without generating gases,[40] dramatically reducing the energy consumption to 242 kJ per mol of CO_2 removed.[37] The energy efficiency can be further improved by introducing a redox-couple in the electrolyte. By adopting the ferricyanide/ferrocyanide redox pair, Digdaya *et al.*[29] demonstrated energy consumptions as low as 155 kJ mol^{-1}. However, the high cost of bipolar membranes might impede the commercialization of the process, and these architectures present risks of toxic redox-couples leaking into the oceanwater.[41]

We describe here a new approach based solely on electrochemical modulation of the pH to initially release the CO_2 and then to alkalize the treated water before it is returned to the ocean. This approach does not require expensive membranes or addition of chemicals, is easy to deploy, and does not lead to formation of byproducts or secondary streams. The CO_2 removal modules can be installed on stationary platforms co-located with wind farms or solar islands in the seas, or on cargo ships plying the oceans; they can also be integrated with on-shore desalination processes to take advantage of the installed water-handling facilities. The captured CO_2 can be injected directly from platforms into sub-surface geologic structures for long term sequestration, or used as a feedstock for fuels or for commodity and specialty chemicals production.

Concept

The pH of ocean water is currently at about 8.1, and most of the inorganic carbon exists in the form of bicarbonate and carbonate ions.[39,42] As noted above, when the concentration of protons in water increases, the bicarbonate and carbonate ions re-speciate to molecular CO_2, which can be then be stripped under vacuum. After the CO_2 removal process is complete, the CO_2-depleted stream can be re-alkalized before being returned to the ocean. The general principles of the process are illustrated schematically in Fig. 1(a), where two electrochemical cells work in tandem. In the first cell, protons are released by one electrode to modulate the pH of the feed stream, while the counter electrode releases chloride ions to ensure charge balance. In the second cell, the reverse reactions occur, with regeneration of the electrodes by storage of protons, recapture of chloride ions, and alkalization of the stream before it is returned to the ocean. In between these steps, molecular CO_2 is stripped under vacuum in a hollow fiber membrane contactor.

Open Access Article. Published on 13 February 2023. Downloaded on 12/27/2024 11:57:29 AM.
This article is licensed under a Creative Commons Attribution-NonCommercial 3.0 Unported Licence.

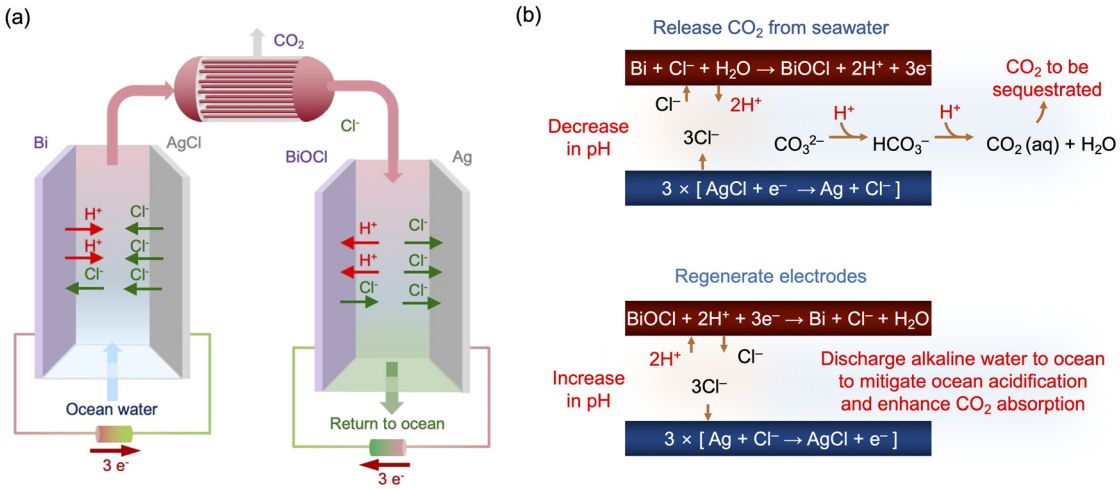

Fig. 1 (a) General principle of the chloride-mediated electrochemical pH swing system for CO_2 removal from ocean water. (b) Electrochemical reactions at bismuth (red) electrode and silver (blue) electrode in each step, and subsequent CO_2 release in the acidified oceanwater.

The cell pair is operated cyclically, with one cell operating until the active electrode is depleted of protons, and the other cell being regenerated as the active electrode is replenished. At the end of a cycle, *i.e.*, when the active electrode is depleted, the flows to each cell are switched, and the polarity of the applied voltages reversed. For this approach, means for the storage and release of H^+ through electrochemical reactions are required. Proton intercalation into metal oxides can be considered,[43–45] but high concentrations of Na^+ present in seawater interfere with H^+ intercalation,[46] making it difficult to use for a pH swing. Therefore, we adopted a method to change the pH that exploits chloride ions present in high concentration in ocean water as a mediator (Fig. 1(b)).

A bismuth (Bi) electrode was used in which Bi reacts under an oxidizing potential to form bismuth oxychloride while releasing protons into the oceanwater feed according to the half reaction:[47]

$$Bi + Cl^- + H_2O \rightleftarrows BiOCl + 2H^+ + 3e^- \quad E^\circ = 0.16\ V\ (vs.\ SHE) \tag{3}$$

Silver chloride (AgCl) was selected as a counter electrode, because of its low overpotential, rapid kinetics, and high capacity for chloride ions. In ocean water, under reducing conditions, AgCl releases chloride ions without impacting the proton concentration, by the following half reaction:[48]

$$AgCl + e^- \rightleftarrows Ag + Cl^- \quad E^\circ = 0.23\ V\ (vs.\ SHE) \tag{4}$$

Based on the stoichiometry of the Bi reaction, two protons are released when three electrons are applied, decreasing the pH of the oceanwater to induce the speciation of the DIC toward molecular CO_2; simultaneously, three chloride ions are released by the AgCl electrode, but one is lost to the formation of BiOCl. The overall reaction can be expressed as

$$Bi + 3AgCl + H_2O \rightleftarrows BiOCl + 3Ag + 2Cl^- + 2H^+ \quad \Delta E^\circ = 0.07\ V \tag{5}$$

From the positive cell potential for the overall reaction, the forward reaction should be spontaneous. Then, on reversal of these reactions, the CO_2-depleted oceanwater can be re-alkalized, giving sufficient alkalinity to ocean water to reabsorb CO_2, while regenerating the electrodes for the next cycle. This approach, which relies on a swing in chloride ion concentration between two different Cl^- capture electrodes, bismuth and silver, to modulate the solution pH, is shown in this paper to have high faradaic efficiency under cyclic flow conditions, with a CO_2 capture energy of 122 kJ mol^{-1}.

Thermodynamic considerations

The desired pH target range for DIC speciation to be primarily toward molecular CO_2 in solution can be assessed through equilibrium concentration calculations of the inorganic carbon species distribution. Here, we consider simulated seawater with a representative composition of 502.5 mM Na^+, 500 mM Cl^-, and varied concentrations of inorganic carbon species to ensure charge neutrality. The concentration of each inorganic carbon species can be calculated based on the acid dissociation constants $K_{a,1}$ and $K_{a,2}$, and on Henry's Law constant K_H, defined as:[49]

$$K_H = \frac{[CO_2(aq)]}{P_{CO_2}} \tag{6}$$

$$K_{a,1} = \frac{a_{H^+} a_{HCO_3^-}}{a_{CO_2}} = \frac{\gamma_{H^+}\gamma_{HCO_3^-}}{\gamma_{CO_2}(aq)} \cdot \frac{[H^+][HCO_3^-]}{[CO_2(aq)]} \tag{7}$$

$$K_{a,2} = \frac{a_{CO_3^{2-}} a_{H^+}}{a_{HCO_3^-}} = \frac{\gamma_{H^+}\gamma_{CO_3^{2-}}}{\gamma_{HCO_3^-}} \cdot \frac{[H^+][CO_3^{2-}]}{[HCO_3^-]} \tag{8}$$

where $[CO_2(aq)]$ is the molar concentration of molecularly dissolved $CO_2(aq)$, P_{CO_2} is partial pressure of CO_2, a_M is the activity of aqueous species M, and γ_M is its activity coefficient ($a_M = \gamma_M[M]$). The equilibrium concentrations of the components are then given by:

 This journal is © The Royal Society of Chemistry 2023

Open Access Article. Published on 13 February 2023. Downloaded on 12/27/2024 11:57:29 AM.
This article is licensed under a Creative Commons Attribution-NonCommercial 3.0 Unported Licence.

$$[CO_2(aq)] = K_H P_{CO_2} \quad (9)$$

$$[HCO_3^-] = \frac{K_{a,1} K_H P_{CO_2} \gamma_{CO_2}(aq)}{\gamma HCO_3^- \gamma_{H^+} [H^+]} \quad (10)$$

$$[CO_3^{2-}] = \frac{K_{a,1} K_{a,2} K_H P_{CO_2} \gamma_{CO_2}(aq)}{\gamma_{CO_3^{2-}} \gamma_{H^+}{}^2 [H^+]^2} \quad (11)$$

The initial concentration of aqueous CO_2 is constant no matter the pH, and is determined by its partial pressure in the ambient air, P_{CO_2}. The concentrations of HCO_3^- and CO_3^{2-}, on the other hand, are strongly affected by the proton concentration, and thus the total dissolved inorganic carbon (DIC) concentration is a function both P_{CO_2} and $[H^+]$:

$$[DIC] = [CO_2(aq)] + [HCO_3^-] + [CO_3^-] \quad (12)$$

The activity coefficients for the charged species were calculated from the Debye–Hückel extension law:

$$\log \gamma_M = -\frac{A z_M^2 \sqrt{I}}{1 + d_M B \sqrt{I}} \quad (13)$$

where A and B are the Debye–Hückel parameters, z_M is the electrical charge of the species, I is ionic strength of the solution, and d_M is the hydrated diameter of the ionic species. The activity of CO_2(aq) was calculated as:

$$\log \gamma_{CO_2(aq)} = \left(C + FT + \frac{G}{T}\right) I - (E + HT) \frac{I}{1 + I} \quad (14)$$

where T is the absolute temperature, C = –1.0312, F = 0.0012806, G = 255.9 K, E = 0.4445, and H = –0.001606 K^{-1}.

As shown in Fig. 2(a), the total DIC of the seawater in equilibrium with the ambient environment is at a concentration of 1.76 mM at pH 8.06, and the relative distributions of HCO_3^- and CO_3^{2-} in this solution are 56% and 43%, respectively, under the ionic strength conditions used here. These values are significantly different from those calculated for ideal solution conditions with all activity coefficients set to unity (Fig. S1, ESI†), where the DIC concentration is larger at 2.5 mM, emphasizing the importance of incorporating the strong effect of ionic strength in thermodynamic analyses of CO_2 speciation in seawater. It is clear that the total DIC solubility decreases sharply with decreasing pH, so that most of the DIC exists as molecular CO_2 when the pH approaches neutral or slightly acidic conditions.

The equilibrium speciation calculated under different charging conditions can be used to estimate the energy requirement for electrochemical modulation of the proton concentration for CO_2 desorption. Under constant current operation, the corresponding release rates of Cl^- and H^+ from the electrodes can be assumed to be constant. Given that net two moles of Cl^- are released when three moles of electron flow in the electric circuit, the concentration of Cl^- as a function of the applied charge Q can be written as

$$[Cl^-] = 0.5M + \frac{3Q}{2V} \quad (15)$$

where V is the volume of the oceanwater treated. On the other hand, Na^+ does not participate in the reactions, and the concentration of Na^+ is constant.

The aqueous feed solution is assumed to be in equilibrium with the ambient environment (containing 420 ppm of CO_2), and thus the concentration of molecular CO_2 is determined by Henry's Law, while $[HCO_3^-]$ and $[CO_3^{2-}]$ are functions of the oceanwater pH, or $[H^+]$, as in eqn (10) and (11). Charge neutrality in the solution will then be satisfied through the balance equation

$$[H^+] + [Na^+] = [Cl^-] + [HCO_3^-] + 2[CO_3^{2-}] + [OH^-] \quad (16)$$

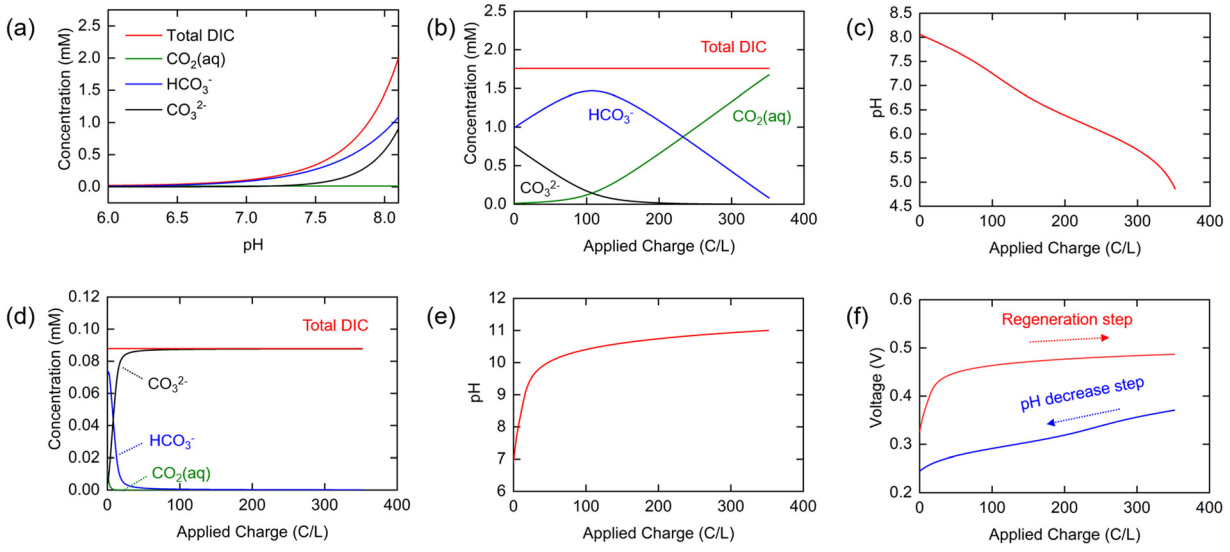

Fig. 2 (a) Equilibrium concentration of inorganic carbon species (CO_2, HCO_3^-, CO_3^{2-}) and total DIC at pH 6–8.1 in simulated seawater and estimated equilibrium concentration of each ionic species in simulated oceanwater in pH decrease step ((b) HCO_3^-, CO_3^{21}, and total DIC, and (c) pH of oceanwater) and in the regeneration step (d) CO_2, HCO_3^-, CO_3^{2-}, and total DIC, and (e) pH during the regeneration step. (e) Equilibrium voltage *vs.* charge curve of chloride-mediated electrochemical pH swing system for CO_2 removal based on the thermodynamic modeling.

Open Access Article. Published on 13 February 2023. Downloaded on 12/27/2024 11:57:29 AM. This article is licensed under a Creative Commons Attribution-NonCommercial 3.0 Unported Licence.

Since $[OH^-]$ is a function of $[H^+]$, as determined by the water dissociation constant ($K_w = 10^{-14}$),[32] and the concentrations of the remaining ionic species are also functions of $[H^+]$, the overall concentration of dissolved inorganic species in the feed introduced to the electrochemical modules can be determined. This total DIC remains constant at $[DIC]_0$ during charging, which impacts only the relative concentrations of the individual inorganic carbon species, which can be determined from

$$[CO_2(aq)] = \frac{[DIC]_0}{1 + \frac{K_{a,1} K_H P_{CO_2} \gamma_{CO_2(aq)}}{\gamma_{HCO_3^-} \gamma_{H^+} [H^+]} + \frac{K_{a,1} K_{a,2} K_H P_{CO_2} \gamma_{CO_2(aq)}}{\gamma_{CO_3^{2-}} \gamma_{H^+}^2 [H^+]^2}} \text{mM} \quad (17)$$

$$[HCO_3^-] = \frac{\left(\frac{K_{a,1} K_H P_{CO_2} \gamma_{CO_2(aq)}}{\gamma_{HCO_3^-} \gamma_{H^+} [H^+]}\right) [DIC]_0}{1 + \frac{K_{a,1} K_H P_{CO_2} \gamma_{CO_2(aq)}}{\gamma_{HCO_3^-} \gamma_{H^+} [H^+]} + \frac{K_{a,1} K_{a,2} K_H P_{CO_2} \gamma_{CO_2(aq)}}{\gamma_{CO_3^{2-}} \gamma_{H^+}^2 [H^+]^2}} \text{mM} \quad (18)$$

$$[CO_3^{2-}] = \frac{\left(\frac{K_{a,1} K_{a,2} K_H P_{CO_2} \gamma_{CO_2(aq)}}{\gamma_{CO_3^{2-}} \gamma_{H^+}^2 [H^+]^2}\right) [DIC]_0}{1 + \frac{K_{a,1} K_H P_{CO_2} \gamma_{CO_2(aq)}}{\gamma_{HCO_3^-} \gamma_{H^+} [H^+]} + \frac{K_{a,1} K_{a,2} K_H P_{CO_2} \gamma_{CO_2(aq)}}{\gamma_{CO_3^{2-}} \gamma_{H^+}^2 [H^+]^2}} \text{mM} \quad (19)$$

The changing distributions in the various components as charge transfer occurs are shown in Fig. 2(b). Of particular interest here is the concentration of molecular aqueous CO_2 as a function of applied charge, as it is this quantity that will determine the conditions needed for effective stripping from the solution post-charging. Note that at low pH with a total $[DIC]_0$ of about 1.8 mM, the fugacity, or effectively the partial pressure, is approximately 0.07 bar, and thus either a vacuum or a sweep gas must be used to strip the CO_2 from the unsaturated solution. The pH is shown as a function of applied charge in Fig. 2(c). Initially, HCO_3^- and CO_3^{2-} exist in a 1 : 0.7 ratio, but the proportion of carbonate quickly decreases$^-$ with a lowering of the pH, to generate primarily HCO_3^-, which then decomposes to form molecular CO_2 (or carbonic acid). Because proton release from the electrode is buffered by these combination reactions with HCO_3^- or CO_3^{2-}, the relatively slow decrease in pH from 8.0 to about 6.0 is expected Fig. 2(c); when most of the HCO_3^- has been consumed, the pH drops rapidly, approaching 5.0.

The reverse process is operative during the regeneration step, in which the concentration of Cl^- increases linearly with applied charge, and $[Na^+]$ again remains constant (Fig. S2b, ESI†). The total DIC concentration is also constant, determined by the residual CO_2 remaining in solution following the stripping step; we set it here as 5% of the initial DIC in oceanwater on the assumption that 95% of the DIC is removed by stripping (*i.e.*, $[DIC]_0$ = 0.1 mM for an initial oceanwater DIC of 2 mM). The calculated concentrations of individual inorganic carbon species during the regeneration step, determined from eqn (17)–(19) with $[DIC]_0$ = 0.1 mM, are shown in Fig. 2(d), while the pH is shown in Fig. 2(e). It was assumed that the same total amount of charge was applied to the cell as in the first step to ensure complete regeneration of the electrodes. As the buffer capacity is low for the CO_2-depleted oceanwater, the pH increases rapidly to 10 and ultimately reaches 11 by the end of the cycle. The proportion of CO_3^{2-} in the DIC increases rapidly at the beginning of this process, reaching 99% when 64 C/L of charge is applied.

The electrochemical thermodynamic cycle can be constructed with the half-cell equilibrium potentials calculated according to the Nernst equation:

$$E = E_0 + \frac{RT}{zF} \ln \frac{a_e a_{ox}}{a_{red}} \quad (20)$$

where E_0 is the standard electrode potential for the reactions, R is the gas constant (8.314 J mol^{-1} K^{-1}), T is the temperature (K), F is the Faraday constant (96 485 C mol^{-1}), and a_e, a_{ox}, and a_{red} represent the activities of electrons, and oxidized and reduced species, respectively. If we assume that the activities of solids and electrons are unity, the electric potential established for the reactions at equilibrium can be expressed by the Nernst equation:

$$E_{Bi}\ (V) = 0.16 + \frac{RT}{nF} \ln \frac{a_{H^+}^2}{a_{Cl^-}} = 0.16 + 0.00856 \ln \frac{a_{H^+}^2}{a_{Cl^-}} \quad (21)$$

$$E_{Ag}\ (V) = 0.23 + \frac{RT}{nF} \ln \frac{1}{a_{Cl^-}} = 0.23 + 0.0257 \ln \frac{1}{a_{Cl^-}} \quad (22)$$

$$E_{Cell}\ (V) = E_{Ag} - E_{Bi} = 0.07 - 0.01714 \ln a_{Cl^-} - 0.01712 \ln a_{H^+} \quad (23)$$

Since the equilibrium electrochemical potentials of the system are determined by the concentrations of H^+ and Cl^-, and these concentrations are dependent on the charge transferred, the equilibrium cell voltages for the pH decrease and electrode regeneration steps will also depend on the applied charge, as plotted in Fig. 2(f). In the absence of an overpotential, the voltage gap between the two steps was found to be significantly below 1 V, with an estimated thermodynamic minimum energy for the process given by

$$W = \frac{F}{NRT} \oint V \mathrm{d}Q \quad (24)$$

of 32 kJ mol^{-1}, where N is the total moles CO_2 captured and released. This value represents a penalty in DIC conversion due to H^+ concentration hysteresis and does not account for the energy for the stripping of the molecular CO_2 from the acidified solution, and for overpotentials required to ensure sufficient driving forces for conversion at finite rates.

Electrode characterization

The material and electrochemical characteristics of the Ag and Bi electrodes employed in the electrochemical system will determine the efficacy of the process. The surface morphologies of the electrodes were observed by SEM. The Ag composite

 This journal is © The Royal Society of Chemistry 2023

Open Access Article. Published on 13 February 2023. Downloaded on 12/27/2024 11:57:29 AM.
This article is licensed under a Creative Commons Attribution-NonCommercial 3.0 Unported Licence.

electrode with surface silver microparticles of 1–2 μm size is shown in Fig. 3(a), while Fig. 3(b) shows the surface structure of the Bi composite electrode prepared with sub-micrometer particle-sized bismuth powders obtained by ball-milling of large (hundreds of micrometers) pristine bismuth particles with conductive carbon (Fig. S2, ESI†). The electrochemical properties of the electrodes under simulated oceanwater conditions were investigated by cyclic voltammetry (CV) analysis. As shown in Fig. 3(c), both electrodes exhibited apparent reversible redox peaks in the solution that were well-matched with those of Ag/AgCl and Bi/BiOCl reactions. The onset potential difference for oxidation and reduction peaks was larger for Bi than for Ag, which might result in higher overpotential requirements. XRD analyses conducted before and after oxidation of the Bi and Ag electrodes in a simulated oceanwater yielded XRD patterns that show clearly that the crystalline structures of Bi and Ag converted to those of BiOCl and AgCl during oxidation (Fig. 3(e) and (f)).

Static cell characterization

The pH swing system was first demonstrated in a static cell either in direct contact with ambient air, so that CO_2 can transfer to and from the solution under alkalization and acidification conditions, respectively, or with release under a nitrogen sweep stream, as illustrated schematically in Fig. 4(a). The bismuth (Bi) and silver chloride (AgCl) electrodes were placed 1 cm apart in 9 mL simulated oceanwater, and the pH and electrochemical potentials of the individual electrodes were monitored throughout the operation. A current of -1 mA cm^{-2} was applied to the electrochemical cell until the

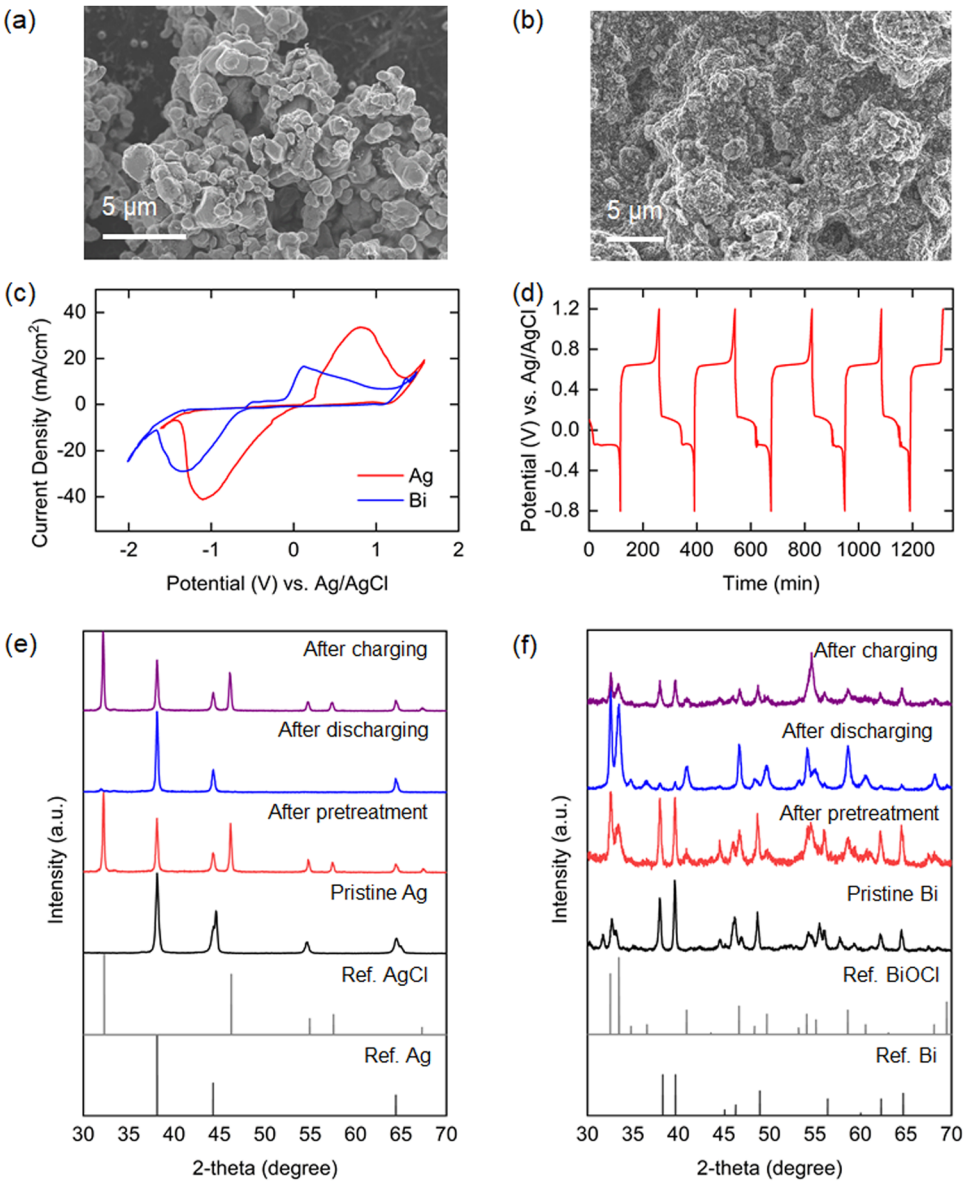

Fig. 3 Material characterization of silver (Ag) and bismuth (Bi) electrodes. SEM images of (a) Ag and (b) Bi, (c) cyclic voltammogram of Ag and Bi, (d) galvanostatic charge/discharge curve of Bi/AgCl cell, and XRD patterns of (e) Ag and (f) Bi after each step.

Open Access Article. Published on 13 February 2023. Downloaded on 12/27/2024 11:57:29 AM.
This article is licensed under a Creative Commons Attribution-NonCommercial 3.0 Unported Licence.

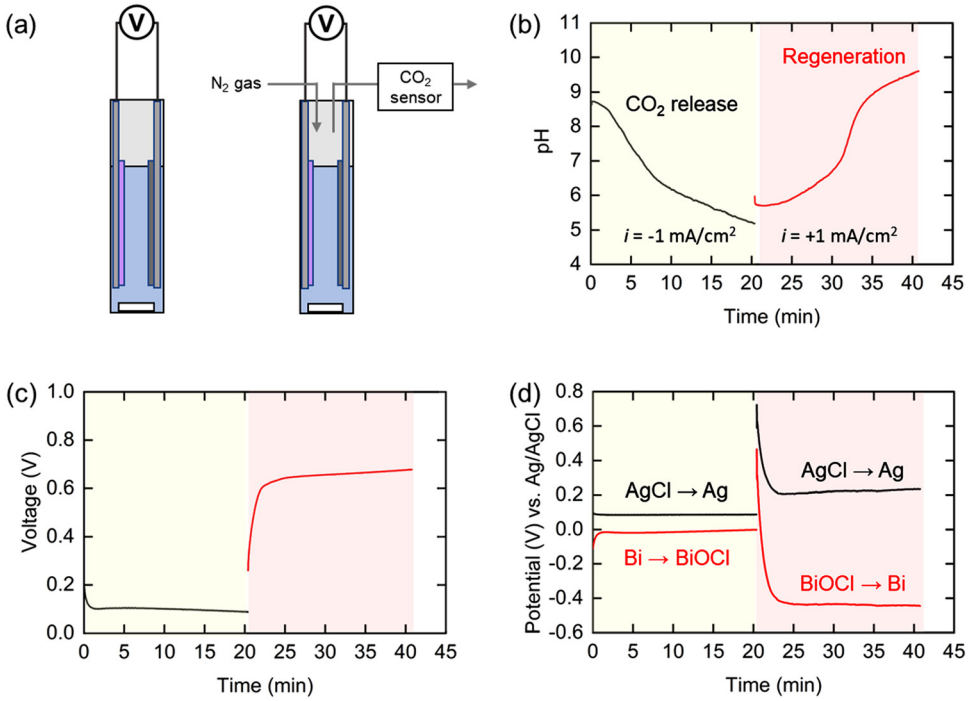

Fig. 4 (a) Schematic illustration of the static cell, and (b–d) electrochemical results and pH profile monitored during CO_2 release step (yellow) and re-alkalization step (pink) in the pH swing operation using a static cell. (b) pH change of the electrolyte, (c) voltage profile, and (d) electrochemical potential of individual electrodes.

total applied charge reached the amount theoretically required to remove 95% of the total DIC. At this point, +1 mA cm^{-2} of current was applied for the same length of time. When the negative current was applied, the pH decreased gently for a short time at the beginning of the operation, before dropping rapidly to a final value of 5.2 (Fig. 4(b)), indicating that the protons were successfully released into the electrochemical cell. This trend is consistent with that estimated by the thermodynamic analysis shown in Fig. 2(c). The initially slow increase in pH in the first half of the second step can be attributed to the residual CO_2 in the solution acting as a buffer. After this residual CO_2 was converted to bicarbonate, the pH rapidly increased to above 9 and another plateau appeared due to the conversion of the bicarbonate to carbonate. Measurements of the concentration of CO_2 in a nitrogen sweep stream used to elute the evolved gas indicated that the diffusion of CO_2 from the solution continued for up to 2 hours following completion of the first step (Fig. S3, ESI†).

The cell voltage (*i.e.*, difference in potentials between the two electrodes) plateaued at 0.1 V in the first step and between 0.6 and 0.7 V in the subsequent step (Fig. 4(c)), resulting in an average voltage gap of 0.55 V between the two steps. Given that the cell voltage of the BPMED in previous reports is usually above 1 V, this suggests that our proposed electrochemical system can be competitive energetically with the state-of-the-art process. The potential at each electrode was also monitored with a reference electrode during the operation (Fig. 4(d)). The electrochemical potential for the silver electrode was 0.1 V and 0.2 V (*vs.* Ag/AgCl) in the first and second steps, respectively, showing 0.1 V of potential difference between the two steps. On the other hand, the potential gap for the bismuth electrode was relatively large, 0.45 V calculated from the values of 0 V and −0.45 V (*vs.* Ag/AgCl) in the first and second steps, respectively. This indicates that the resistance due to the Bi/BiOCl reaction, which is significantly larger than that of the Ag/AgCl reaction, is the primary determinant of the energy consumption in this system. Given that the standard potential of Bi is −0.05 V (*vs.* Ag/AgCl), the reaction kinetics for the Bi to BiOCl oxidation is quite fast. On the other hand, the kinetics for the reduction reaction (BiOCl to Bi) is sluggish as water dissociation should be involved in the reaction mechanism to generate H^+.

Continuous flow cyclic operation

For practical demonstration of the electrochemical Cl^- swing proton modulation process, it will be necessary to implement these concepts in a continuous swing mode of operation. The ocean water entering the electrochemical modules needs to undergo three steps: (1) acidification to release CO_2, (2) stripping of CO_2 into a gaseous phase, and (3) re-alkalization to regenerate the electrodes for the next swing cycle. For these purposes, two cells were prepared with identical compositions (bismuth and silver) but in different oxidation states: Bi/AgCl for Cell 1 and BiOCl/Ag for Cell 2. As shown in Fig. 5(a), the oceanwater passed through the two cells consecutively with acidification of the oceanwater in Cell 1, and alkalization of the acidified water in Cell 2 once the CO_2 had been stripped in a hollow fiber membrane contactor by a nitrogen sweep gas used

 This journal is © The Royal Society of Chemistry 2023

Open Access Article. Published on 13 February 2023. Downloaded on 12/27/2024 11:57:29 AM.
This article is licensed under a Creative Commons Attribution-NonCommercial 3.0 Unported Licence.

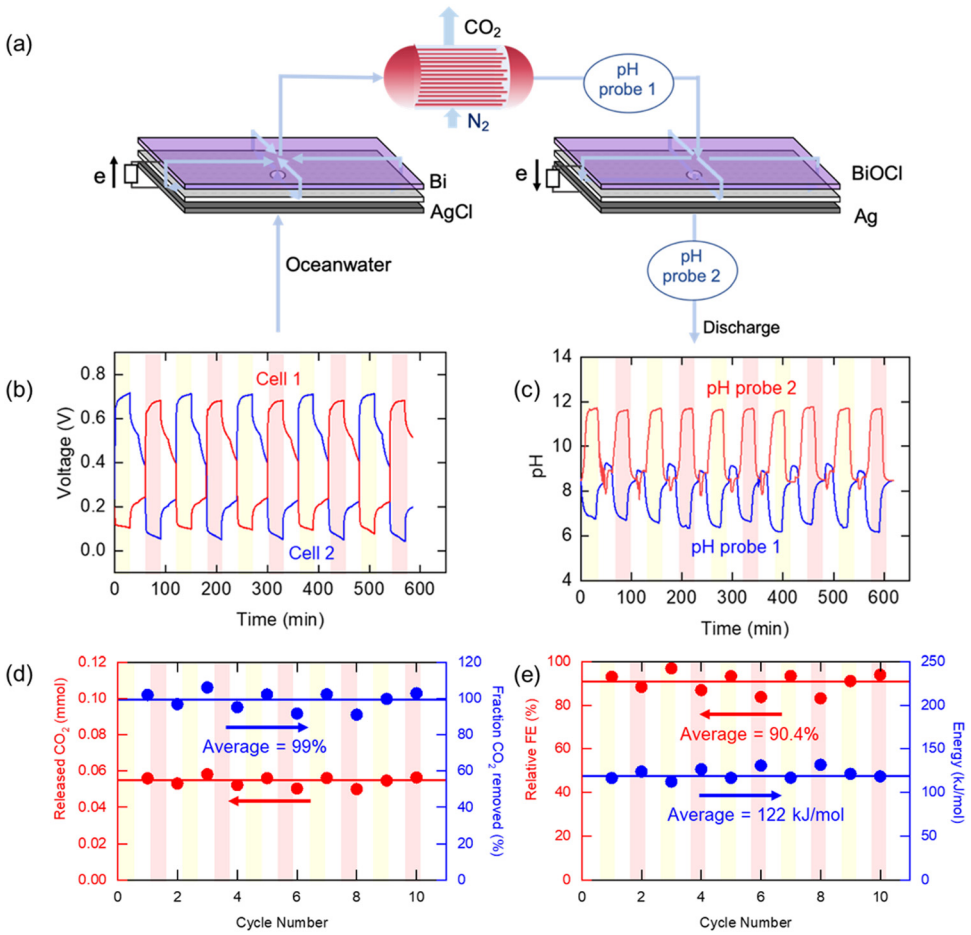

Fig. 5 (a) Schematic illustration of the continuous electrochemical cell and (b–e) profiles monitored during the continuous electrochemical pH swing process operation for 10 cycles. (b) Voltage and (c) pH of the effluents from two cells. (d) Molar amount of released CO_2 (red, left) and fraction of CO_2 removed (blue, right). (e) Relative Faradaic efficiency (red, left) and energy consumption (blue, right) during the operation of continuous process for 10 cycles.

to emulate vacuum degasification of the water in which the CO_2 fugacity (partial pressure) is only $\sim$0.07 bar. The water was pumped to Cell 1 at a flow rate of 1.04 mL min^{-1}, in which 99.3% of DIC could be removed from the oceanwater if the faradaic efficiency were to be 100%. CO_2 removal was tracked by measuring the concentration of CO_2 in the nitrogen sweep gas (5 mL min^{-1}), and the pH of the CO_2-depleted stream was monitored to evaluate the system performance. The water then entered Cell 2, in which the pH of the oceanwater increased by the reverse reactions of Cell 1. The pH of the effluent from Cell 2 was also monitored before discharge. After 30 min, the system was allowed to rest under the same flow conditions, with no current applied, before the operation mode was changed to the second step, in which the roles of the two cells were switched such that the oceanwater flowed in the opposite direction, sequentially passing through Cell 2 and then through Cell 1. The CO_2 in the simulated oceanwater could be removed continuously by repeating these steps, discharging water with increased alkalinity.

Fig. 5(b) shows the measured voltage when the system operated under constant current conditions. A negative current (-1 mA cm^{-2}) was applied for 30 minutes to Cell 1 to decrease pH in the ocean water, while a positive current (+1 mA cm^{-2}) was applied for same amount of time to Cell 2 to increase the pH of CO_2-depleted oceanwater. During the operation, the voltage of the charging cell was maintained at 0.7 V, while that of discharging cell was about 0.1 V. The voltage gap between two cells was 0.6 V on average, which is similar to the result shown for the static cell. Fig. 5(c) shows the pH profile during the operation. The pH of the effluent from the cells operating in the acidification mode decreased to 6, indicating that the ocean water was acidified, while in the regeneration cells the pH approached 12, as anticipated. The pH profiles were similar no matter which of the two cells was being used for acidification, and there was no observable decline in performance over ten cycles. When the acidified oceanwater passed through the membrane contactor, the CO_2 was stripped out by the nitrogen sweep stream; there was a rapid increase in the measured CO_2 concentration to 8000–10 000 ppm in the sweep stream when the current was applied to the electrochemical cells, as shown in Fig. S6 (ESI†), from which the average amount of CO_2 removed per cycle of 0.0543 mmol, shown in Fig. 5(d), could

Open Access Article. Published on 13 February 2023. Downloaded on 12/27/2024 11:57:29 AM.
This article is licensed under a Creative Commons Attribution-NonCommercial 3.0 Unported Licence.

be calculated, indicating that 87% of the DIC was removed from the oceanwater These calculations allowed for the fact that a small amount of CO_2 (about 500 ppm) was released even during the rest period when no current was applied, which was subtracted from the concentration of CO_2 released during the operation when estimate the amount of released CO_2 in each step that could be attributed to pH modulation. Meanwhile, the pH measured in the re-alkalizing cell effluent reached about 10–11, which is consistent with the thermodynamic calculation (Fig. 2(e)). This value is much higher than the pH of the initial oceanwater, which was about 8, owing to the reduction in buffering capacity after most of the DIC was removed from solution. After discharge of the effluent into the ocean, the solution will be restored to pH $\sim$8, the typical pH of oceanwater, by absorbing CO_2 from the atmosphere.

Fig. 5(e) shows the relative faradaic efficiency (η) and the energy consumption during operation. Based on the stoichiometry of the electrochemical reactions, the theoretical maximum FE is 67%, as two protons are released for every 3 electrons applied to the system. Therefore, the relative η was defined as the η divided by the theoretical maximum η $\left(\eta_{rel} = \frac{\eta}{\eta_{max}}\right)$. During the 10-cycle operation, the average relative FE was 90.4%, and 122 kJ mol^{-1} of energy was expended, on average. Compared to previous studies that had electrochemical energy consumption of more than 155 kJ mol^{-1}, our proposed system is energetically competitive at the applied current densities, with the caveat that these current densities are lower than those used in earlier studies; further development of this process may require increased current densities to reduce total electrode area needed.

The contents of bismuth and silver in the effluent were measured by ICP-MS. No bismuth was detected in the effluent solution, but the content of silver was 0.255 mg L^{-1}. Means for the amelioration of this slow loss of silver will need to be addressed through identification either of other electrode compositions, or of methods to prevent the dissolution of the silver electrode.

Additional tests were carried out using synthetic seawater with the same composition as seawater. As shown in Fig. S7 (ESI†), the amount of released CO_2 decreased over the 4-cycle operation, dropping to 31% in the second cycle and further decreasing to 13% after four cycles relative to the first cycle. The reason for the rapid decrease is attributed to possible $Mg(OH)_2$ formation on the electrode surface owing to the high local surface pH relative to that in the bulk flow. This pH difference is due to the establishment of a concentration boundary layer to balance the concentration-driven proton fluxes with the applied reducing current. With a lowered current density (+0.125 mA cm^{-2}) in the regeneration step, the pH difference between the bulk and surface was reduced, and hence also the precipitation of fouling compounds such as $Mg(OH)_2$, culminating in a 96% performance retention in the second cycle and 67% in the fourth. Strategies to enhance the overall stability of these electrochemical systems under more realistic conditions are clearly needed, and will be a focus of our future studies.

Transport modelling

The importance of transport phenomena on system performance was evaluated using a COMSOL Multiphysics model developed to determine ion distributions during flow cell operation. The simulated flow cell geometry was simplified to a 2D axisymmetric domain of an equal active surface area (6.25 cm^2) and gap size (3 mm) as the experimental cell, and simulations were conducted under the same flow rate conditions (1 ccm). Physics were governed by coupling the time-dependent Nernst–Planck equations to a steady state flow profile. DIC interconversion was modelled pointwise by homogeneous rate laws.[42] Electrodes were modelled as 2D electrode surfaces governed by Butler–Volmer kinetics, with externally applied potentials varied to elicit a steady state current density of 0.9 mA cm^{-2} (corresponding to an experimental 1 mA cm^{-2} with 90% faradaic efficiency). Electrolyte inlet compositions were selected to match simulated seawater (pH 8.1, 2 mM DIC) during acidification, and post-treatment water (pH 6, 0.1 mM DIC) during regeneration. Additional model parameters are detailed in the ESI.†

Fig. 6(a) shows the COMSOL abstraction of the experimental flow cell, reduced to an equivalent 2D axisymmetric domain to minimize computational intensity while retaining essential transport characteristics. Fig. 6(b) illustrates the corresponding pH distributions during acidification and alkalization operations, with the *r*-coordinate compressed by a factor of 10 for clearer visualization. Due to the sluggish kinetics of conversion from HCO_3^- to CO_2 relative to H^+ diffusion timescales, a sharp reaction front can be observed during forward operation, dividing the channel into a highly acidic (pH $\sim$ 3.5) top region near the Bi electrode and a region of unaffected seawater near the Ag counter electrode. Prior to alkalization, 95% of DIC buffering capacity has been removed from the cell, resulting in a much smoother pH profile, with inhomogeneities primarily owing to recirculation effects near the inlet.

Fig. 6(c) illustrates the dependence of cell potential on pH experienced at the bismuth electrode, highlighting notable values in the system. Losses in performance due to variations in open circuit potential throughout the channel can be formulated as a concentration overpotential:

$$\eta_k = |\Delta\Phi_{eq}([H]_{surf}) - \Delta\Phi_{eq}([H]_{bulk})| \quad (25)$$

Fig. 6(d) indicates the total measured overpotential experienced by the bismuth electrode in the real system relative to the inlet conditions, compared to average calculated concentration overpotentials relative to the inlet and channel cross section. Acidification calculations suggest that a significant portion of the Bi overpotential during this step might be due to an excess concentration of protons at the bismuth surface, whereas spatial variations in concentration likely only account for only a small portion of the re-alkalization overpotential. Mixing is therefore an important consideration in a real system, as improving the spatial uniformity of conversion of DIC to CO_2 at a pH closer to 6 could improve energetics in the acidification step.

 This journal is © The Royal Society of Chemistry 2023

Open Access Article. Published on 13 February 2023. Downloaded on 12/27/2024 11:57:29 AM.
This article is licensed under a Creative Commons Attribution-NonCommercial 3.0 Unported Licence.

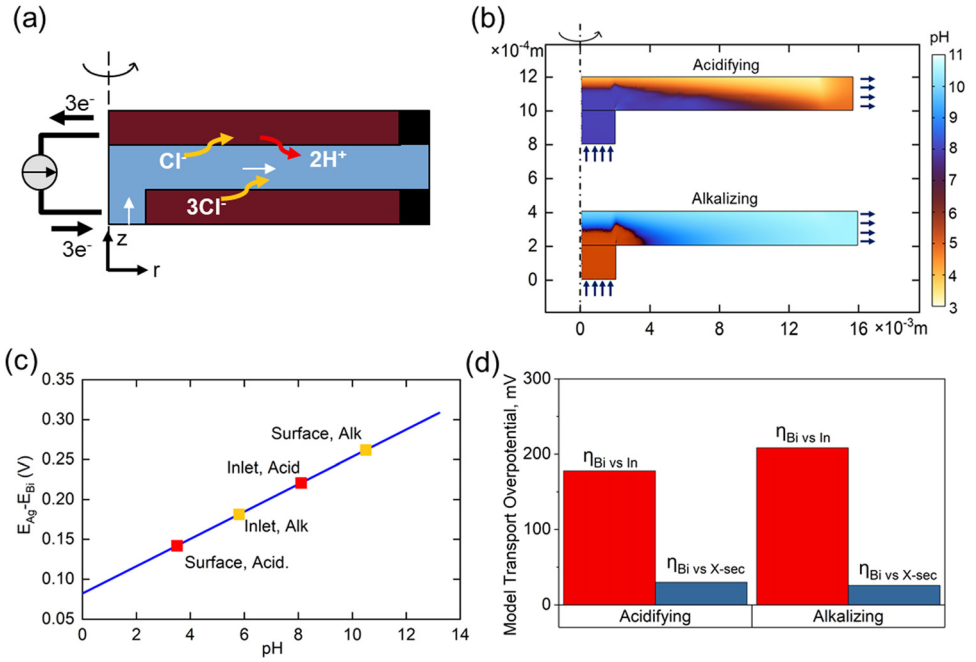

Fig. 6 COMSOL transport model and results (a) simulated flow cell geometry during acidification (b) pH profile of the simulated cell during steady state operation (c) dependence of open circuit potential on pH (d) total measured Bi/BiOCl overpotential (η_{Tot}) in the flow cell compared to model predictions of polarization overpotential relative to inlet (η_{Inlet}) and polarization relative to average cross section pH ($\eta_{x\text{-}sec}$)

Overall performance of modules

The thermodynamic model described earlier can be used to estimate the impact of current density and flow rates in the modules. Consider a module illustrated schematically in Fig. 7(a) of cross-sectional area S (m^2) and length L (m), with flow channels occupying a fraction of this volume, the remainder being the electrode materials themselves. The volumetric rate at which seawater is treated is $m^3\ s^{-1}$, while the current density is I ($C\ m^{-2}\ s^{-1}$); the total electrode area per unit volume of module is given by ($m^2\ m^{-3}$). The applied charge Q ($C\ m^{-3}$) in the flowing seawater at point z in the module is obtained from the balance equation

$$vQ = Ia\varepsilon Sz \tag{26}$$

which can be rearranged to give the axial location at which the given amount of charge has been transferred, *i.e.*, at which the effective charge accumulation is Q:

$$\zeta = \frac{z}{L} = \frac{v}{Ia\varepsilon SL} \quad Q = \frac{1}{Ia\tau_{res}} \quad Q \tag{27}$$

where $\tau_{res} = \varepsilon SL/v$ is the residence time of the fluid in the module. Thus, we can re-formulate the results given in Fig. 2 for pH and concentration of molecular CO_2 as functions of Q to show how these quantities will vary with position ζ in the module for various values of $Ia\tau_{res}$, which is the total charge accumulation per unit volume of treated water. The profiles in Fig. 7(b) and (c) showing the variation in molecular CO_2 and pH, respectively, with position during the acidification process can be used to determine the residence times (and hence module size) required to attain a desired conversion of DIC to molecular CO_2 for a given current density, or the current density required to treat a given amount of water in an existing module. Note that for some values of $Ia\tau_{res}$ full conversion of the DIC is attained fairly early in the unit, and the remainder of the module is not utilized effectively. An appropriate value for $Ia\tau_{res}$ can be obtained from the plot of the exit CO_2 concentration *vs.* $Ia\tau_{res}$ as shown in Fig. 7(d) and will depend on the desired exit concentration. A total applied charge of between 3 and 4 $\times$ 10^6 C m^{-3} would be sufficient to convert the DIC in ocean water almost completely to molecular CO_2 in the contactor.

We can use a similar analysis to look at the regeneration modules, and explore scenarios for the reduction of the final pH in these modules. In many cases, it would be desirable to ensure that the pH did not reach levels of 9.5 or greater at which precipitates of, say, $Mg(OH)_2$, form, which may foul the electrodes and reduce the overall efficiency of the process. A strategy to overcome this limitation would be to mix the decarbonated solution with fresh oceanwater as shown in Fig. 7(e) so that the residence time restrictions can be disentangled from the current density needs, and, moreover, the buffering capacity of the bicarbonate solution may limit the overall increase in pH. In Fig. 7(f) we illustrate the results from such a mixing of the acidified, decarbonated stream with fresh oceanwater in different proportions, which has the effect of increasing slightly the pH of the feed to the regeneration unit, but also decreases the required residence time in the unit for constant total charge transferred (*i.e.*, constant Ia). With increasing addition of ocean water, the pH of the regeneration

Open Access Article. Published on 13 February 2023. Downloaded on 12/27/2024 11:57:29 AM.
This article is licensed under a Creative Commons Attribution-NonCommercial 3.0 Unported Licence.

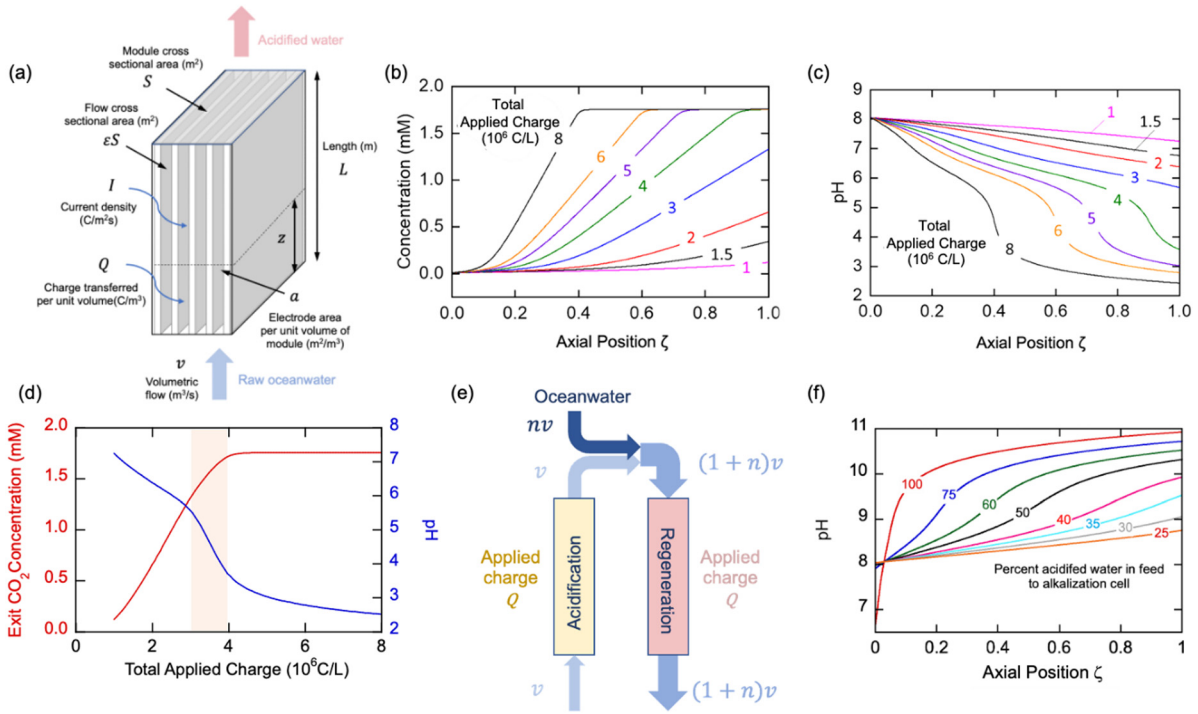

Fig. 7 Overall module performance. (a) Schematic of cell module, (b) and (c) axial concentration and pH profiles for different total amounts of charge applied, (d) Molecular CO_2 concentration and pH of stream leaving module depending on total applied charge, (e) Schematic showing mixing of acidified stream with fresh ocean water for regeneration cycle, (f) Axial pH profiles for different additions of oceanwater to acidified water.

stream decreases, which is the desired effect. Since this increase in volumetric flow to the unit would be at the expense of added pumping costs, however. This simple model provides added insight into different operational strategies, but will need to be augmented with more detailed analyses that account for transport and other kinetic limitations within the cells, a topic for future studies.

Technoeconomic analysis and optimization

A detailed technoeconomic analysis (TEA) was performed to explore the economic viability and cost drivers of the asymmetric electrochemical pH-swing DOC approach when implemented at commercial scale. While a complete DOC system requires oceanwater intake, degasification, and compression systems,[29,37] this analysis focuses on the systems specific to the electrochemical pH-swing approach developed herein. It is important to note that the asymmetric chlorine-mediated pH swing process is not expected to substantially change the operating requirements of the pre-filtration and subsequent degassing steps when compared to alternative methods of acidification (see ESI†). Thus, other analyses can provide estimates for the expected vacuum degassing, filtration, and auxiliary costs outside of the electrochemical system for a complete system involving the asymmetric cells.[29,37,38]

For the electrochemical system, cost estimates for the cell stack capital expenditures (CAPEX), cell stack electricity costs, and pumping capital and operating costs are shown in Fig. 8(a). The CAPEX of the Bi/AgCl electrode cell stack at scale is estimated using alkaline water electrolyzer costs adjusted for our process specifics. Cell electricity costs are calculated using the experimental 122 kJ mol^{-1}-CO_2 as the base required energy and adding ohmic losses through the electrolyte which become relevant at high current densities and large cell gaps. Pumping investment and operating costs are calculated given the flow rate and pressure drop through the cells. Detailed calculations and assumptions can be found in ESI.†

The model cell stack operational current density and electrode gap are varied in the TEA as shown in Fig. 8(b), highlighting some key physical system design tradeoffs. At low current densities, large electrode areas are required and cause cell CAPEX costs to dominate. Beyond 76 mA cm^{-2}, additional benefits from increasing current density are outweighed by increased ohmic losses through the oceanwater and increased pumping costs due to higher required flow velocities. Pumping costs dominate for slim electrode gaps, while ohmic losses drive costs at large electrode gaps, resulting in an optimum at 1.1 mm. The minimized system cost at these optimized parameters is \$56 per tCO_2 with cost components shown in Fig. 8(c).

The balancing act between the current density, gap width, and pumping costs is generalizable to all electrochemical DOC systems with flow between parallel electrodes, including electrodialysis systems. A notable effect of this interplay is the constraint of the current density to a value much lower than the >1 A cm^{-2} typically sought for large-scale industrial electrochemical plants.[50–53] The inflexibly low conductivity of oceanwater and extremely high required oceanwater throughput are fundamental characteristics which elevate the relevance of electrolyte ohmic losses and limitations on the cell gap for

 This journal is © The Royal Society of Chemistry 2023

Open Access Article. Published on 13 February 2023. Downloaded on 12/27/2024 11:57:29 AM.
This article is licensed under a Creative Commons Attribution-NonCommercial 3.0 Unported Licence.

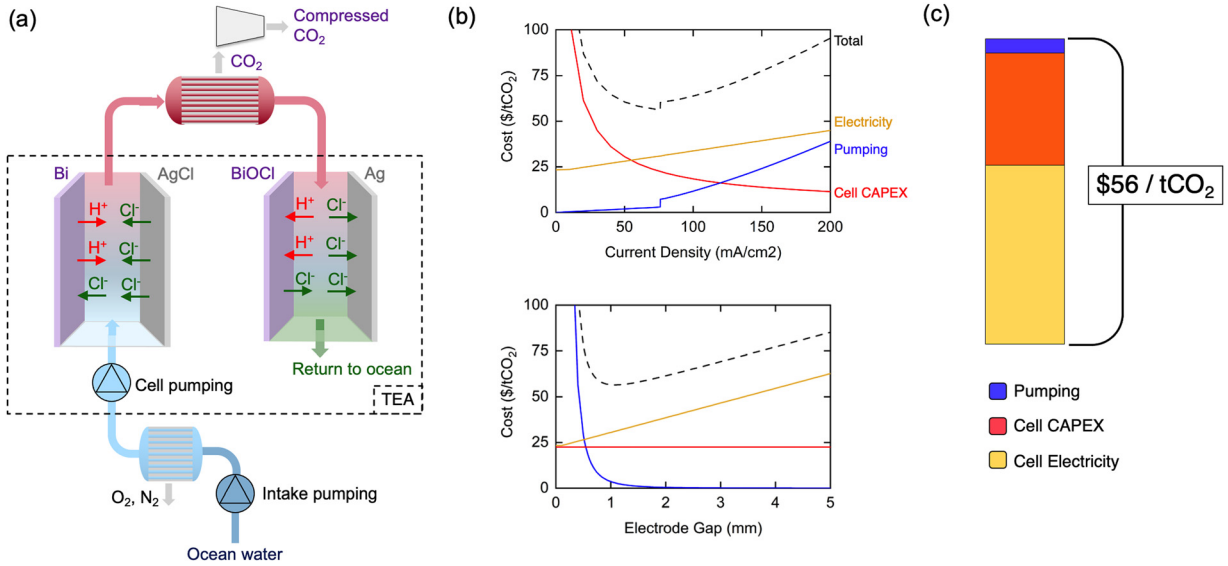

Fig. 8 (a) Complete DOC system including intake systems, gas separations, and compression. The scope of this TEA is shown by the dashed box, including cell stack costs, electricity, and pumping. (b) System cost optimization of cell current density and inter-electrode gap. When current density is varied, electrode gap is fixed at 1.1 mm. When electrode gap is varied, current density is fixed at 76 mA cm^{-2}. (c) System cost components at a current density of 76 mA cm^{-2} and an inter-electrode gap of 1.1 mm where total costs are minimized at \$56 per tCO_2.

current DOC systems compared to other large-scale electrochemical technologies. To the best of our knowledge, this effect has not been explored in previous technoeconomic or system analyses, which assume operation at higher current densities in excess of 100's of mA cm^{-2}.

However, these physical tradeoffs reveal avenues for continued system cost reduction. Moving away from parallel-electrode architectures towards alternatives such as inter-digitated electrodes could decouple the opposing nature of electricity costs and pumping costs. With such a design, larger cell gaps which minimize pumping costs could be attained while keeping ohmic losses low and allowing higher current density operation. Though our base energy consumption of 122 kJ mol^{-1}-CO_2 is a record-low, it may still be substantially decreased towards the thermodynamic limit of 32 kJ mol^{-1}-CO_2. Finally, high cell stack CAPEX costs at low current densities motivate the development of electrodes which operate efficiently at higher current densities by mitigating the overpotentials shown in our transport modeling.

The \$56 per tCO_2 initial cost estimate of our asymmetric electrochemical pH-swing system is comparable to that of electrodialysis system costs under the same assumptions.[29] The promising energetics of our process yield lower cell electricity costs, though our initial investment CAPEX estimates are slightly higher (see ESI† Note S3). However, our analysis does not account for replacements and O&M costs which we expect to be significantly lower for our system involving only two electrodes, no redox couples, and no membranes which typically require frequent replacement. The reduced part count and simplicity of our system is promising for its scalability.

Our electrochemical system cost estimates fall within commonly accepted targets of \$100 per tCO_2,[54] but other system costs are critical to evaluate as well. Previous analyses indicate that intake filtration, pumping and gas separation costs may incur total process costs as high as \$2000 per tCO_2.[29,37] At present, these costs dominate those associated with the electrochemical system and motivate further work in reducing degassing costs and pumping costs in addition to electrochemical improvements.

Conclusions

The chloride-mediated electrochemical pH swing system in this proof-of-concept study provides a new method to achieve negative emissions by removing CO_2 from seawater without the use of expensive bipolar membranes or the need for specific anolytes and catholytes to drive the reactions in the electrode cells. In contrast to previously reported electrodialysis systems, the chloride-mediated electrochemical pH swing system is used to modulate the pH of oceanwater, and hence the speciation of the DIC, by reversible electrochemical reactions at the electrodes instead of by water dissociation in the bipolar membranes. These advances are possible through adoption of two different electrodes, bismuth and silver, that capture chloride ions. Continuous CO_2 removal from simulated oceanwater was demonstrated by combining two silver–bismuth systems and showed robust behavior over 10 hours of operation. Removal of 87% of the DIC in the simulated oceanwater was observed, with 92% relative faradaic efficiency and 122 kJ mol^{-1} energy consumption. The bismuth electrode is inexpensive and can robustly modulate the pH of chloride-containing salt water regardless of the type and concentration of cations. On the other hand, although silver has the advantage of large capacity and low energy penalty, electrode dissolution will need to be overcome by modifying the silver particles or replacing silver

Open Access Article. Published on 13 February 2023. Downloaded on 12/27/2024 11:57:29 AM.
This article is licensed under a Creative Commons Attribution-NonCommercial 3.0 Unported Licence.

with another material; this is to be the subject of future studies. Methods to overcome the fouling of electrodes during the regeneration step owing to local high surface pH conditions that promote the formation of precipitates such as $Mg(OH)_2$ must be developed, and several engineering and electrochemical approaches are currently being considered to alleviate the fouling issues; one such method was discussed in which the degasified water was mixed with fresh ocean water before being fed to the regeneration cell to reduce the overall pH increase in the flow channel.

For convenience, in the small demonstration unit a nitrogen sweep gas was used to emulate the drawing of a vacuum for disengagement of the CO_2 (at a fugacity of $\sim$0.07 bar) from the acidified water, since the partial pressure of CO_2 in the sweep stream will be on a par with the actual pressure of pure CO_2 obtained under vacuum degasification at, say 0.01 bar. As with other published processes for CO_2 removal from ocean waters, this low-pressure CO_2 would need to be compressed either for use as a feedstock for production of chemicals, materials and fuels, or for sequestration in sub-surface geologic formations.

The techno-economic analysis shows that this ocean capture system can be economically feasible with costs ranging from \$50–\$100 per ton CO_2 depending on the current applied and the gap between electrodes, and could be lowered to \$56 per ton CO_2 under optimized conditions. However, these calculations only considered the economic feasibility of the electrochemical system itself, and it is necessary to perform an integrated analysis, including other equipment such as intake systems, gas separations, and compression.

Experimental

Preparation of electrodes

The electrodes were prepared by mixing 80 wt% bismuth powder (Alpha Aesar), 10 wt% carbon black (Super P, Timcal), and 10 wt% polyvinylidene fluoride (PVDF, Sigma Aldrich) binder. Before the fabrication, the bismuth and carbon black were ball-milled together for 1 h to reduce particle size and increase the contact between bismuth and carbon powder. The mixture was dispersed in an organic solvent (*N*-methyl-2-pyrrolidone, NMP), and cast on a graphite sheet (200 μm of thickness) using the doctor blade method. The silver electrode was fabricated by mixing silver powder (Sigma Aldrich), carbon black (Super P, as conducting agent), and polytetrafluoroethylene (PTFE) binder (8 : 1 : 1 by weight, respectively) in ethanol. The mixture was placed in a roll pressor and a sheet-type electrode was obtained with 200 μm of thickness. Both electrodes were dried in an oven overnight to remove the residual solvent.

Characterization of the electrodes

The surface morphology of the electrodes was characterized by field emission scanning electron microscopy (FE-SEM, Zeiss MERLIN). The crystalline structure was analyzed by X-ray diffraction (XRD, Rigaku) in a 2θ range of 10–80° with a ramping step of 5° min^{-1}. Cyclic voltammetry (CV) analyses were carried out to determine the electrochemical properties of the electrodes in 0.5 M NaCl and 2.5 mM $NaHCO_3$ solution in a three-electrode cell. A platinum wire was used as a counter electrode and a commercial Ag/AgCl (3 M KCl) was applied as a reference electrode. The CV scan was obtained by a potentiostat (PAR) with scan rates of 2 mV s^{-1}.

CO_2 removal experiments

The flow-type CO_2 removal cell was assembled with the silver chloride as a positive electrode and bismuth as a negative electrode. A pair of graphite sheets ($\sim$200 μm of thickness) was used as current collectors to connect the electrodes to the potentiostat. The silver electrode was cut into a square shape (2.5×2.5 cm^2) with a 3 mm hole located at the center to make a flow channel between the electrodes. The bismuth electrode was also cut into a square shape without any hole. For the flow channel, two nylon spacers ($\sim$100 μm) and one filter paper ($\sim$200 μm) were placed between the electrodes. For the test, a simulated oceanwater containing 0.5 M of NaCl and 2.5 mM of $NaHCO_3$ was pumped into the cell at a flow rate of 1.04 mL min^{-1} with a peristaltic pump. Two pH micro electrodes (8220BNWP, thermo fisher) were connected to the flow channel to monitor the pH of the effluents from each cell, and the data were acquired with isoPods (eDAQ). A membrane contactor was used to promote the CO_2 release from water into a flowing nitrogen sweep stream, which was used to emulate the drawing of a vacuum on the unit. A CO_2 sensor (CO_2 Meter) was connected right after the membrane contactor to measure the concentration of CO_2 in the gas phase. The content of silver and bismuth in the effluent was analyzed with ion-coupled plasma-mass spectroscopy (ICP-MS, Agilent). For this measurement, the effluent and 5 M nitric acid solution were mixed in a 6 : 4 volume ratio.

Conflicts of interest

There are no conflicts to declare.

Acknowledgements

This work was supported under ARPA-E Grant DE-AR0001409.

References

1 *IPCC, IPCC special report on carbon dioxide capture and storage*, Cambridge University Press, New York, 2005.
2 M. Bui, C. S. Adjiman, A. Bardow, E. J. Anthony, A. Boston, S. Brown, P. S. Fennell, S. Fuss, A. Galindo, L. A. Hackett, J. P. Hallett, H. J. Herzog, G. Jackson, J. Kemper, S. Krevor, G. C. Maitland, M. Matuszewski, I. S. Metcalfe, C. Petit, G. Puxty, J. Reimer, D. M. Reiner, E. S. Rubin, S. A. Scott, N. Shah, B. Smit, J. P. M. Trusler, P. Webley, J. Wilcox and N. Mac Dowell, *Energy Environ. Sci.*, 2018, **11**, 1062–1176.

 This journal is © The Royal Society of Chemistry 2023

Open Access Article. Published on 13 February 2023. Downloaded on 12/27/2024 11:57:29 AM. This article is licensed under a Creative Commons Attribution-NonCommercial 3.0 Unported Licence.

3 P. Folger, *Science*, 2009, **325**, 1652–1654.
4 M. Wang, A. Lawal, P. Stephenson, J. Sidders and C. Ramshaw, *Chem. Eng. Res. Des.*, 2011, **89**, 1609–1624.
5 M. C. Stern, F. Simeon, H. Herzog and T. A. Hatton, *Energy Environ. Sci.*, 2013, **6**, 2505–2517.
6 N. Mac Dowell, P. S. Fennell, N. Shah and G. C. Maitland, *Nat. Clim. Change*, 2017, **7**, 243–249.
7 Y. Wang, L. Zhao, A. Otto, M. Robinius and D. Stolten, *Energy Procedia*, 2017, **114**, 650–665.
8 F. M. Orr, *Science*, 2009, **325**, 1656–1658.
9 K. Hashimoto, *Global Carbon Dioxide Recycling for Global Sustainable Development by Renewable Energy*, Springer, Singapore, 2019, pp.5–17.
10 D. W. Keith, *Science*, 2009, **325**, 1654–1655.
11 T. Gasser, C. Guivarch, K. Tachiiri, C. D. Jones and P. Ciais, *Nat. Commun.*, 2015, **6**, 7958.
12 J. Hansen, M. Sato, P. Kharecha, K. Von Schuckmann and D. J. Beerling, *Earth Syst. Dyn.*, 2017, **8**, 577–616.
13 E. S. Sanz-Pérez, C. R. Murdock, S. A. Didas and C. W. Jones, *Chem. Rev.*, 2016, **116**, 11840–11876.
14 D. W. Keith, G. Holmes, D. St. Angelo and K. Heidel, *Joule*, 2018, **2**, 1573–1594.
15 S. Voskian and T. A. Hatton, *Energy Environ. Sci.*, 2019, **12**, 3530–3547.
16 M. Obersteiner, C. Azar, S. Kossmeier, R. Mechler, K. Mollersten, S. Nilsson, P. REad, Y. Yamagata and J. Yan, *IIASA Interim Rep.*, 2001, 1–23.
17 F. Creutzig, N. H. Ravindranath, G. Berndes, S. Bolwig, R. Bright, F. Cherubini, H. Chum, E. Corbera, M. Delucchi, A. Faaij, J. Fargione, H. Haberl, G. Heath, O. Lucon, R. Plevin, A. Popp, C. Robledo-Abad, S. Rose, P. Smith, A. Stromman, S. Suh and O. Masera, *GCB Bioenergy*, 2015, **7**, 916–944.
18 C. Halliday and T. A. Hatton, *Ind. Eng. Chem. Res.*, 2020, **59**, 22582–22596.
19 B. Locatelli, C. P. Catterall, P. Imbach, C. Kumar, R. Lasco, E. Marín-Spiotta, B. Mercer, J. S. Powers, N. Schwartz and M. Uriarte, *Restor. Ecol.*, 2015, **23**, 337–343.
20 J. Busch, J. Engelmann, S. C. Cook-Patton, B. W. Griscom, T. Kroeger, H. Possingham and P. Shyamsundar, *Nat. Clim. Change*, 2019, **9**, 463–466.
21 P. Landschützer, N. Gruber and D. C. E. Bakker, *Global Biogeochem. Cycles*, 2016, **30**, 1396–1417.
22 N. Gruber, D. Clement, B. R. Carter, R. A. Feely, S. van Heuven, M. Hoppema, M. Ishii, R. M. Key, A. Kozyr, S. K. Lauvset, C. Lo Monaco, J. T. Mathis, A. Murata, A. Olsen, F. F. Perez, C. L. Sabine, T. Tanhua and R. Wanninkhof, *Science*, 2019, **363**, 1193–1199.
23 S. C. Doney, V. J. Fabry, R. A. Feely and J. A. Kleypas, *Annu. Rev. Mater. Sci.*, 2009, **1**, 169–192.
24 C. D. Harvell, P. F. Sale, A. J. Edwards, K. Caldeira, N. Knowlton and C. M. Eakin, *Science*, 2007, **318**, 1737–1743.
25 A. D. Moy, W. R. Howard, S. G. Bray and T. W. Trull, *Nat. Geosci.*, 2009, **2**, 276–280.
26 F. Gazeau, C. Quiblier, J. M. Jansen, J. P. Gattuso, J. J. Middelburg and C. H. R. Heip, *Geophys. Res. Lett.*, 2007, **34**, 1–5.
27 C. Content, *Oceans and the Atmospheric Carbon Content*, 2011.
28 F. J. Millero, *Chem. Rev.*, 2007, **107**, 308–341.
29 I. A. Digdaya, I. Sullivan, M. Lin, L. Han, W. H. Cheng, H. A. Atwater and C. Xiang, *Nat. Commun.*, 2020, **11**, 1–10.
30 H. D. Willauer, F. DiMascio, D. R. Hardy and F. W. Williams, *Energy Fuels*, 2017, **31**, 1723–1730.
31 R. Sharifian, R. M. Wagterveld, I. A. Digdaya, C. Xiang and D. A. Vermaas, *Energy Environ. Sci.*, 2021, **14**, 781–814.
32 V. Snoeyink and D. Jenkins, *Water Chemistry*, John Wiley & Sons, New York, 1st edn, 1980.
33 M. D. Eisaman, J. L. B. Rivest, S. D. Karnitz, C. F. de Lannoy, A. Jose, R. W. DeVaul and K. Hannun, *Int. J. Greenhouse Gas Control*, 2018, **70**, 254–261.
34 H. D. Willauer, F. Dimascio, D. R. Hardy and F. W. Williams, *Ind. Eng. Chem. Res.*, 2014, **53**, 12192–12200.
35 S. Jin, M. Wu, R. G. Gordon, M. J. Aziz and D. G. Kwabi, *Energy Environ. Sci.*, 2020, **13**, 3706–3722.
36 K. M. Diederichsen, R. Sharifian, J. S. Kang, Y. Liu, S. Kim, B. M. Gallant, D. Vermaas and T. A. Hatton, *Nat. Rev. Methods Primers*, 2022, **2**, 68.
37 M. D. Eisaman, K. Parajuly, A. Tuganov, C. Eldershaw, N. Chang and K. A. Littau, *Energy Environ. Sci.*, 2012, **5**, 7346–7352.
38 C. F. de Lannoy, M. D. Eisaman, A. Jose, S. D. Karnitz, R. W. DeVaul, K. Hannun and J. L. B. Rivest, *Int. J. Greenhouse Gas Control*, 2018, **70**, 243–253.
39 B. D. Patterson, F. Mo, A. Borgschulte, M. Hillestad, F. Joos, T. Kristiansen, S. Sunde and J. A. van Bokhoven, *Proc. Natl. Acad. Sci. U. S. A.*, 2019, **116**, 12212–12219.
40 R. Pärnamäe, S. Mareev, V. Nikonenko, S. Melnikov, N. Sheldeshov, V. Zabolotskii, H. V. M. Hamelers and M. Tedesco, *J. Membr. Sci.*, 2021, **617**, 118538.
41 C. Du, J. R. Du, X. Zhao, F. Cheng, M. E. A. Ali and X. Feng, *Ind. Eng. Chem. Res.*, 2021, **60**, 3115–3129.
42 R. E. Zeebe and D. Wolf-Gladrow, *CO_2 in seawater: Equlibrium, kinetics, isotopes,* Elsevier Science B.V., 1st edn, 2001.
43 M. Rahimi, G. Catalini, S. Hariharan, M. Wang, M. Puccini and T. A. Hatton, *Cell Rep. Phys. Sci.*, 2020, **1**, 100033.
44 M. Rahimi, G. Catalini, M. Puccini and T. A. Hatton, *RSC Adv.*, 2020, **10**, 16832–16843.
45 T. Kim, B. E. Logan and C. A. Gorski, *Environ. Sci. Technol. Lett.*, 2017, **4**, 49–53.
46 V. Augustyn, P. Simon and B. Dunn, *Energy Environ. Sci.*, 2014, **7**, 1597–1614.
47 D. H. Nam and K. S. Choi, *J. Am. Chem. Soc.*, 2017, **139**, 11055–11063.
48 A. J. Bard and L. R. Faulkner, *Electrochemical methods: Fundamentals and applications*, John Wiley & Sons, New York, 2nd edn, 2001.

Open Access Article. Published on 13 February 2023. Downloaded on 12/27/2024 11:57:29 AM.
This article is licensed under a Creative Commons Attribution-NonCommercial 3.0 Unported Licence.

49 P. Atkins and J. de Paula, *Atkins' physical chemistry*, Oxford university press, Oxford, 10th edn, 2014.
50 S. Shiva Kumar and V. Himabindu, *Mater. Sci. Energy Technol.*, 2019, **2**, 442–454.
51 A. Villagra and P. Millet, *Int. J. Hydrogen Energy*, 2019, **44**, 9708–9717.
52 J. B. Todd, *JOM*, 1981, **33**, 42–45.
53 J. I. Otashu and M. Baldea, *Comput. Chem. Eng.*, 2019, **121**, 396–408.
54 Office of Fossil Energy and Carbon Management, Carbon Negative Shot, **https://www.energy.gov/fecm/carbon-negative-shot**, (accessed 24 October 2022).

 This journal is © The Royal Society of Chemistry 2023